An improved pixel-based water vapor tomography model

Yibin Yao [1,2,*], **Linyang Xin** [1] **and Qingzhi Zhao** [3]

[1] School of Geodesy and Geomatics, Wuhan University, Wuhan 430079, China;
ybyao@whu.edu.cn (Y.Y); linyangxin@whu.edu.cn (L.X);

[2] Key Laboratory of Geospace Environment and Geodesy, Ministry of Education, Wuhan University, Wuhan 430079, China

[3] College of Geomatics, Xi'an University of Science and Technology, Xi'an 710054, China;
zhaoqingzhia@163.com

* Correspondence: ybyao@whu.edu.cn; Tel.: +86-027-68758401

Abstract: As an innovative use of Global Navigation Satellite System (GNSS), GNSS water vapor tomography technique shows great potential in monitoring three-dimensional water vapor variation. Most of the previous studies employ the pixel-based method, i.e., dividing the troposphere space into finite voxels and considering water vapor in each voxel as constant. However, this method cannot reflect the variations in voxels and breaks the continuity of the troposphere. Moreover, in the pixel-based method, each voxel needs a parameter to represent the water vapor density, which means huge numbers of parameters are needed to represent the water vapor field when the interested area is large and/or the expected resolution is high. In order to overcome abovementioned problems, in this study, we propose an improved pixel-based water vapor tomography model, which uses layered optimal polynomial functions obtained from the European Centre for Medium-Range Weather Forecasts (ECMWF) by adaptive training for water vapor retrieval. Tomography experiments were carried out using the GNSS data collected from the Hong Kong Satellite Positioning Reference Station Network (SatRef) from March 25 to April 25, 2014 under different scenarios. The tomographic results are compared to the ECMWF data and validated by the radiosonde. Results show the new model outperforms the traditional one by reducing the Root Mean Square Error (RMSE) and this improvement is more pronounced by 5.88% in voxels without the penetration of GNSS rays. The improved model also has advantages in expression with more convenience.

Keywords: GNSS; water vapor tomography; ECMWF; Radiosonde

1. Introduction

As the most active component in the troposphere, water vapor is one of the most difficult parameters to monitor and describe (Rocken et al., 1997). A good understanding of the spatial-temporal variation of water vapor is very helpful for improving weather forecasting and early warning of disastrous weather (Weckwerth et al., 2004).

The GNSS technique can not only retrieve the precipitable water vapor (Bevis et al., 1994; Emardson et al., 1998; Baltink et al., 2002; Bock et al., 2005) but also monitor the three-dimensional water vapor distribution by using the GNSS tomography method (Flores et al., 2000; Seko et al., 2000; Macdonald et al., 2002).

Braun et al. (1999) first proposed the concept of reconstructing the tropospheric water vapor structure using 20 GPS stations in a regional observational network. Flores et al. (2000) first applied the tomography technique to obtain wet refractivity from the GNSS slant wet delay (SWD). In the same year, Hirahara (2000) used a different method to conduct GNSS tomography experiments, which also successfully obtained three-dimensional water vapor fields. Since then, many scientists proposed new methods and applied them to GNSS water vapor tomography experiments (Rohm et al., 2014; Yao et al., 2016; Zhang et al., 2017; Ding et al., 2018; Zhao et al., 2018).

Hirahara (2000) conducted a four-dimensional tomography experiment and solved the tomography equations using the damping least square method. Braun et al. (2003, 2004) overcame the sensitivity problem in GNSS tomography by using the extended sequential filtering method. Perler et al. (2011) presented a new parametric method for the water vapor retrieval. Nilsson and Gradinarsky (2006) obtained the wet refractivity directly from the GNSS phase observations using the Kalman filter method. Rohm and Bosy (2009) used the Moore-Penrose pseudo-inverse of variance-covariance to solve the linear equations and emphasized the ill-posed tomography equation. Yao et al. (2016) obtained good tomographic results by using the optimal grid-making method. Zhao and Yao (2017) proposed a method of using the side-penetrating signals for tomography and improved the utilization rate of the GNSS rays. Aghajany and Amerian (2017) obtained the tomography results of water vapor profiles from ERA-I numerical weather prediction data by applying 3D ray tracing technique. Dong and Jin (2018) reconstructed the water vapor density using multi-GNSS systems and showed that the accuracy of GNSS tomography results are improved by 5% from the GPS-only system to the dual-systems (GPS+GLONASS). Besides, the virtual reference station approach (Marel, 1998; Vollath et al., 2013), an effective method to attenuate the effects of atmospheric errors in long-distance dynamic positioning, was also used in GNSS tropospheric tomography.

In previous studies, most of the GNSS tomography methods divided the interested troposphere into finite voxels and the water vapor density in each voxel is considered as constant, these methods with the above assumptions are defined as the pixel-based method. Apparently, this kind of method cannot retrieve the variations in voxels and breaks the continuous nature of the troposphere as well. Moreover, the pixel-based method requires each voxel to have a parameter to represent the water vapor density in it, which may lead to the situation that we have to use huge numbers of parameters when the research area is large and the expected resolution is high. Last, over-parametrization may cause mathematical problems when we use limited observations to invert for the parameters that may be correlated. Therefore, this paper analyzes the limitations of the traditional pixel-based water vapor tomography method and proposes an improved model. The improved model uses the water vapor density obtained from the traditional model as the input value and outputs the fitting water vapor density by the layered optimal polynomial functions. This new model

74 has the advantages of reflecting the variations in voxels and keeping the continuity of water vapor in

75 troposphere.

2. An improved pixel-based water vapor tomography model

2.1. Establishment of the traditional pixel-based water vapor tomography model

2.1.1. Retrieval of SWV

79   For tropospheric tomography, the most important observation is the slant water vapor (SWV), which

80 is related to the water vapor density and can be defined by

$$SWV = \int_S \rho_V ds \quad (1)$$

82 where *s* represents the path of the satellite signal ray, and ρ_V is the water vapor density (units: g/m^3).

83 SWV can be obtained by the following method:

$$SWV = \frac{10^6}{R_\omega [(k_3 / T_m) + k_2^{'}]} \cdot SWD \quad (2)$$

85 where $k_2^{'}$=16.48 K hPa^{-1}, k_3=3.776×10^5 K^2 hPa^{-1}, and R_ω=461 J kg^{-1} K^{-1}, which represent the specific

86 gas constants for water vapor. T_m is the weighted mean tropospheric temperature, calculated from an

87 empirical equation proposed by Liu et al. (2001) using the meteorological measurements. SWD is the slant

88 wet delay, which may be given as

$$SWD_{elv,\varphi} = m_{wet}(elv) \times ZWD + m_{wet}(elv) \times \cot(elv) \times (G_{NS}^w \times \cos\varphi + G_{EW}^w \times \sin\varphi) + R \quad (3)$$

90 where *elv* is the satellite elevation, φ is the azimuth, m_{wet} is the wet mapping function, G_{NS}^w and G_{EW}^w

91 are the wet delay gradient parameters in the north-south and east-west directions, respectively. *R* refers to

92 the unmodeled zero difference residuals that may involve unmodeled influence on the three-dimensional

93 spatial water vapor distribution, which can make up for the lack of tropospheric anisotropy using only the

94 gradient term (Bi et al., 2006). Since the GAMIT software only provides the double difference residuals,

95 the zero difference residuals in this paper are obtained from the double difference residuals according to

96 the method proposed by Alber et al. (2000). ZWD is the zenith wet delay, which is extracted from the zenith

97 tropospheric delay (ZTD) by separating the zenith hydrostatic delay (ZHD) using equation ZWD=ZTD-

98 ZHD. ZHD can be calculated precisely using surface pressure based on the Saastamoinen model

99 (Saastamoinen, 1972):

$$ZHD = \frac{0.002277 \times P_s}{1 - 0.00266 \times \cos(2\varphi) - 0.00028 \times H} \quad (4)$$

101 where P_s is the surface pressure (unit: hPa), φ is the latitude of the station, and H is the geodetic

102 height (unit: km). The unit of ZHD is meter.

103   Since the SWV is obtained, the tomographic area can be discretized into a number of voxels, in which

104 the water vapor density is a constant during a given period of time. Therefore, a linear equation relating the

105 SWV and the water vapor density can be established as follows (Chen and Liu, 2014):

106

$$SWV^{p} = \sum_{ijk}(D_{ijk}^{p} \cdot \rho_{ijk}) \quad (5)$$

107

108   where SWV^{p} is the slant water vapor of ρ th signal path (unit: mm). i, j, and k are the positions of

109   discrete tomographic voxels in the longitudinal, latitudinal and vertical directions, respectively. D_{ijk}^{p} is

110   the distance of the ρ th signal in voxel (i, j, k) (unit: km). ρ_{ijk} is the water vapor density in a given voxel

111   (i, j, k) (unit: g/m^3). A matrix form of this observation equation can be rewritten as follows (Flores et al.,

112   2000; Chen and Liu, 2014):

113

$$y_{m \times 1} = A_{m \times n} \cdot \rho_{n \times 1} \quad (6)$$

114   where m is the number of total SWVs, and n is the number of voxels in the tomographic area. y is the

115   observed value here as the SWV, which penetrates the whole interest area, A is the coefficient matrix of the

116   signal transit distances through the voxels, and ρ is the column vector of the unknown water vapor

117   density.

118   2.1.2. Constraint equations of the tomography modeling

119   Solving for the unknown water vapor density in Eq. (6) is actually an inversion algorithm issue as the

120   design matrix A is a large sparse matrix, whose normal equation is singular, leading to numerical problems

121   when using a direct inversion method (Bender et al., 2011). To overcome this rank deficiency problem,

122   constraint equations are often introduced to the tomography equation (Flores et al., 2000; Troller et al.,

123   2002; Rohm and Bosy, 2009; Bender et al., 2011). In our study, the horizontal constraint equation is imposed

124   by the Gauss-weighted functional method (Guo et al., 2016) and the vertical constraint equation is imposed

125   by the functional relationship of the exponential distribution (Cao, 2012), respectively. The final

126   tomography model is then obtained as

127

$$\begin{pmatrix} A_{m \times n} \\ H_{m \times n} \\ V_{m \times n} \end{pmatrix} \cdot \rho_{n \times 1} = \begin{pmatrix} y_{m \times n} \\ 0_{m \times n} \\ 0_{m \times n} \end{pmatrix} \quad (7)$$

128   where H and V are the coefficient matrices of horizontal and vertical constrains, respectively. In order to

129   obtain the inverse matrix shown in Eq. (7), singular value decomposition is used in this paper (Flores et al.,

130   2000).

131   *2.2. An improved pixel-based water vapor tomography model*

132   The improved pixel-based water vapor tomography model proposed in this paper can take advantage

133   of facilitating the continuity of water vapor expression efficiently in spatial-temporal distribution and

134   calculating the water vapor density conveniently. The improved tomography model firstly obtains the water

135   vapor density from voxels penetrated by GNSS rays using the traditional pixel-based tomography model,

136   then obtains the optimal polynomial function of each layer through adaptive training. With known

137   coefficients of the layered optimal polynomial functions, the water vapor density can finally be calculated

138   by given the latitude, longitude and the altitude. Specific steps are as follows:

139   First, use the traditional pixel-based water vapor tomography model to obtain the initial water vapor

140   density from voxels penetrated by GNSS rays as the observation values for obtaining the optimal

141   polynomial function coefficients of each layer.

142   Second, normalize the coordinates of each voxel center in the tomographic area. Since the polynomial

143   fitting of the water vapor at each tomographic layer is in essence to establish the relationship between the

144   latitude as well as the longitude of the tomographic region and the water vapor density. The general

145   expression is:

146
$$V_d = a_0 + a_1 B + a_2 L + a_3 BL + a_4 B^2 + a_5 L^2 + a_6 B^2 L \cdots \quad (8)$$

147   where B is the latitude, L is the longitude, and V_d represents the water vapor density. Polynomial

148   coefficients such as a_i are obtained via the least squares method. In the process of data solving, the

149   numerical values of the latitude and longitude may not be small, then the magnitude of multiple power may

150   be larger than 10^4, which will lead to the ill-posed problem of the design matrix in the inversion process

151   and eventually affect the reliability of the estimated coefficients. To ensure the design matrix will be

152   relatively stable in the inversion process, the latitude and longitude coordinates B and L need to be

153   normalized. The specific methods are as follows:

154
$$B^* = \frac{B - \mu_B}{\sigma_B}$$
$$L^* = \frac{L - \mu_L}{\sigma_L} \quad (9)$$

155   where B^* and L^* are the normalized latitude and longitude, respectively, and B and L are the

156   latitude and longitude in the initial region range. μ is the average value of the latitude or longitude, and

157   σ is the standard deviation of the latitude or longitude.

158   Third, determine the layered optimal polynomial functions of the improved model through adaptive

159   training.

160   •   First, based on the size of the selected tomographic region, determine the highest

161   polynomial fit order. In this paper, the highest polynomial fit order chosen as 5 turns out to

162   be generally sufficient.

163   •   Then set the water vapor density from voxels penetrated by GNSS signal rays as the input

164   value and keep trying out new polynomial functions, the optimal polynomial function of

165   each layer is obtained by adaptive training. What needs to be noted here is the number of

166   estimated coefficients need to be less than that of the voxels penetrated by GNSS rays in

167   each layer. Otherwise the over-fitting problem would happen.

168   •   Finally, after comparing training results of multi-group polynomial functions at different

169   levels, the polynomial function with the minimum RMSE value obtained from the water

170   vapor density of the post-fitting layer and that of the ECMWF is the best fitting equation

171   for this layer. Each layer could have the individual optimal polynomial function in general.

172   Fourth, after finding the optimal polynomial function of each layer in different heights, taking the

173   latitude, longitude and altitude information into the function could obtain the three-dimensional water vapor

174   distribution in the tomographic region. The continuous water vapor density can be easily described by

175   broadcasting the estimated coefficients of the layered optimal polynomial functions.

176 *2.3. The optimal polynomial selection based on adaptive training*

177   Since the polynomial form can well reflect the continuity of water vapor and has the advantage of
178 high-efficiency computing as well as easy expression, this paper chooses the polynomial form as the layered
179 fitting function. Based on adaptive training, the selection process of the layered optimal polynomial
180 function is as follows:

181   First, construct a polynomial equations training library, which contains a wide variety of polynomial
182 function forms of the latitude and longitude as independent variables while of the water vapor density in
183 the voxels as the dependent variable. After many experiments, the maximum power of the latitude and
184 longitude found as 5 is sufficient to describe the water vapor changes. Therefore, the maximum power of
185 the fitting function part is adopted as 5 in the training library.

186   Second, according to the water vapor density observations from the voxels penetrated by the GNSS
187 signals at each level, the form of the candidate polynomial function of each layer is automatically
188 determined from the polynomial function training library, ensuring that the number of observations at all
189 levels is always greater than that of estimated coefficients of candidate polynomials.

190   Third, calculate the water vapor variation index (WVVI) of each layer in both east-west and north-
191 south directions using the traditional water vapor tomography results as shown in Eq. (10).

192
$$WVVI = \frac{\overline{\nabla wv_{EW}}}{\overline{\nabla wv_{NS}}} \tag{10}$$

193 where wv_{EW} and wv_{NS} are the water vapor density in east-west and north-south direction, separately.

194   The WVVI is a changing rate indicator of the water vapor density in a given direction. According to
195 the water vapor variation index of each layer in the east-west and north-south direction, it can be determined
196 whether the water vapor exists mainly in the east-west distribution or the north-south distribution. As an
197 aid, WVVI can decide the main body of the alternative polynomial function with higher order whether in
198 longitude or latitude and then efficiently find the layered optimal polynomial function. If the water vapor
199 density of a layer indicates a horizontal gradient of east-west distribution, the polynomial function with
200 higher-order term of the longitude should be given the priority. It suggests that when the water vapor shows
201 an east-west gradient distribution there is a better correlation between the longitude and the water vapor
202 variation, furthermore the high-order term in longitude can better reflect the nuanced water vapor variation.
203 A simple example of the polynomial function with a higher-order term in longitude is shown in Eq. (11):

204
$$V_d = a_0 + a_1 B + a_2 L + a_3 BL + a_4 L^2 + a_5 BL^2 + a_6 L^3 \tag{11}$$

205   Otherwise, when the water vapor density of a layer indicates a horizontal gradient of north-south
206 distribution, the polynomial function with higher-order term of the latitude should be given the priority. A
207 simple example is shown in Eq. (12):

208
$$V_d = a_0 + a_1 B + a_2 L + a_3 BL + a_4 B^2 + a_5 B^2 L + a_6 B^3 \tag{12}$$

209   While the distribution regularities of the water vapor density gradient are not clear or obvious, the
210 polynomial function with the same order of the latitude and longitude can be considered as the example
211 shown in Eq. (13):

212
$$V_d = a_0 + a_1 B + a_2 L + a_3 BL + a_4 B^2 + a_5 L^2 \tag{13}$$

213   Fourth, the candidate polynomials of all levels screened by the WVVI gradient auxiliary information
214   are used as the next comparative polynomials, and the required estimated coefficients of the comparative
215   polynomial are solved according to the principle of least squares through Eq. (14) and automatically
216   recorded into the coefficients data set. M is the matrix of the longitude and latitude, and the vector x
217   comprises the unknown coefficients of the comparative polynomial functions as shown in Eq. (15).

218    $$V_d = Mx \qquad (14)$$

219    $$x = \begin{bmatrix} a_0 \\ a_1 \\ \vdots \\ a_n \end{bmatrix} \qquad (15)$$

220   Fifth, through the comparative polynomials with the estimated coefficients in each layer, the whole-
221   voxel water vapor fitting of each layer is automatically fit with the information of the latitude and longitude.
222   In order to obtain the RMSE, the fitting result would be compared with the ECMWF water vapor density
223   of each layer in this period. The results are then saved to the accuracy data sets of each layer. The
224   comparative polynomials with the estimated coefficients are constantly selected to train the fitting of the
225   layered water vapor density and then compared with the water vapor density of ECMWF at each layer.
226   Thus, large accuracy data sets of RMSE can be obtained, where the smallest RMSE value of the
227   comparative polynomial form can be chosen, and then the optimal polynomial of each layer could come
228   into being. It is noteworthy that the optimal polynomial of each layer might be different. With the layered
229   optimal polynomial, the continuous three-dimensional water vapor density in the tomographic region can
230   be expressed conveniently by transmitting the estimated coefficients information.

231   **3. Experiment**

232   *3.1. Experimental description and data-processing strategy*

233   To study whether the accuracy and stability of the improved water vapor tomography model are better
234   than that of the traditional model, the following experiment is designed.

235   Tomographic data is obtained from the SatRef Network for Hong Kong from 25 March 2014 to 25
236   April 2014. Two epochs are taken each day (0:00 and 12:00 UTC). The corresponding meteorological data
237   is also used to calculate the PWV. The tomographic area ranges between latitude 22.24°N to 22.54°N and
238   longitude 113.87°E to 114.29°E. Taking the mean sea level as the height of the base level, the vertical
239   resolution is 0.8 km, and total grid number is $5 \times 7 \times 13$. In the selected area, a total of 11 GNSS stations
240   and 1 radiosonde station (located at King's Park, Hong Kong) are selected, and the ECMWF grid data are
241   extracted twice daily at 00:00 and 12:00 UTC from 25 March 2014 to 25 April 2014 (grid resolution of
242   0.125×0.125). See Fig. 1 for details.

243
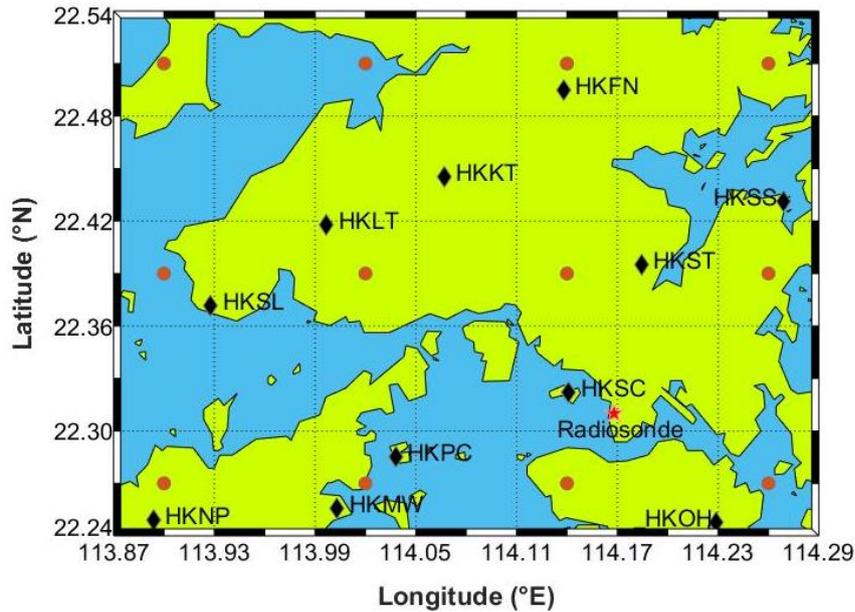
◆ GNSS Station ★ Radiosonde ● ECMWF

244

245 **Figure 1.** The GNSS stations (11 black rhombuses) and the radiosonde station (1 red star) and the ECMWF comparative

246 points (12 ochre circles) in Hong Kong. The grid lines display tomography grids.

247 According to the official website of the Hong Kong Observatory

248 (http://www.weather.gov.hk/contentc.htm) for the weather review, Hong Kong had a total of 15 days of

249 rainy weather from 25 March 2014 to 25 April 2014, as shown in Table 1.

250

Table 1. Rainfall information for March and April 2014.

Date	Rainfall situation
3.29	Thunderstorms turn to heavy rain
3.30	Thunderstorms turn to heavy rain
3.31	Thunderstorms turn to heavy rain
4.1	Showers accompanied by wind, thunderstorms
4.2	Showers, reports of hail in some areas
4.3	Showers, some parts of the rain are quite large
4.6	Cloudy showers, low temperature
4.7	Heavy showers, low temperature
4.8	Showers, low temperature
4.14	Showers
4.21	Cloudy turns to the showers
4.22	Showers and foggy
4.23	Showers turn to the rain
4.24	Showers turn to the cloudy
4.25	Cloudy turns to the rain

251 In this paper, GAMIT (v10.50) (Herring et al., 2010) software was used for processing the GPS

252 observations based on the double-differenced model at a sampling interval of 30 s, and the global mapping

253 function was adopted. The zenith total delay (ZTD) and wet horizontal gradient intervals were estimated at

254 0.5 h and 2 h, respectively. Based on the surface pressure obtained from observed meteorological

255 parameters, the ZHD could be obtained by the Saastamoinen model, and ZWD was isolated from ZHD.
256 Via GMF projection, the SWD could be obtained by transforming the observed SWV.

3.2. Experimental introduction and comparison

258 The RMSE and bias of the improved tomography model residuals were calculated by subtracting the
259 ECMWF water vapor density from the water vapor density of the improved pixel-based water vapor
260 tomography model (hereinafter referred to as the improved model). In a similar way, the RMSE and bias of
261 the traditional tomography model residuals can also be obtained from the difference between the ECMWF
262 water vapor density and the water vapor density obtained by the traditional pixel-based water vapor
263 tomography model (hereinafter referred to as the traditional model).

264 In order to evaluate the improved model, this paper investigates 6 scenarios, comprising the spatial
265 distribution scenario, the everyday distribution scenario, the rainy scenario and the non-rainy scenario.
266 Moreover the scenarios of residuals of the water vapor density in voxels with and without penetrating GNSS
267 rays are inspected. The definitions of 6 scenarios abovementioned are as follows:

268 The spatial distribution scenario is investigated by obtaining the RMSE and bias of the residuals from
269 all ECMWF comparative points at all time intervals.

270 The everyday distribution scenario is found by obtaining the RMSE and bias of the residuals from all
271 ECMWF comparative points in two epochs each day. Besides the overall accuracy of 32 days between 25
272 March 2014 and 25 April 2014 was calculated.

273 The rainy scenario is based on 15 rainy days between 25 March and 25 April, 2014, as referred to in
274 Table 1. The RMSE and bias of the residuals are obtained from all ECMWF comparative points in all the
275 epochs during rainy days. Similarly, the non-rainy scenario is found with the accuracy analysis of the
276 non-rainy days.

277 The scenario of residuals of the water vapor density in voxels without GNSS rays penetration is found
278 by obtaining the RMSE and bias of the residuals from ECMWF comparative points without rays passing
279 through in all the epochs each day. Conversely, the scenario with GNSS rays penetration is found by
280 obtaining the RMSE and bias of the residuals from ECMWF comparative points with rays penetrating in
281 all the epochs each day.

282 According to the above classifications, the accuracy of the improved model residuals and the
283 traditional model residuals were calculated, and the accuracy of the improved model was compared with
284 the traditional one to find out which one is better. Furthermore, the water vapor comparison with radiosonde
285 data was designed to show if the improved model would be more efficient than the traditional one.

4. Interpretation of 6 scenario results

4.1. Accuracy information of the spatial distribution scenario

288 To verify whether the accuracy of the improved model is better than that of the traditional model, the
289 layered RMSE and bias of the residuals are obtained from the tomography results (using both the optimal
290 polynomial function of each layer and the traditional way) and the ECMWF data in all ECMWF
291 comparative points (shown in Table 2). The calculation of RMSE improvement percentage involved in the
292 following tables is shown in Eq. (16).

$$\Delta RMSE\% = \left(RMSE_{trad} - RMSE_{impr} \right) / RMSE_{trad} \cdot 100\% \quad (16)$$

294 where $RMSE_{impr}$ is the RMSE value of the residuals calculated from the improved model, and

295    $RMSE_{trad}$ is the RMSE value of the residuals obtained from the traditional model.

296   Table 2 shows that RMSE and bias values obtained by the improved model are smaller than those of
297   the traditional model, and the RMSE improvement percentage is positive, which indicates that the improved
298   model has a higher accuracy than the traditional model in general. The reason of the appreciable RMSE
299   improvement percentage in the upper region is that the value of the water vapor density in high altitudes is
300   very small (see Fig. 2 for details), even small water vapor changes could cause a large percentage fluctuation.
301   In addition, the bias and RMSE in the bottom from Table 2 are not as good as those of the other higher
302   layers, regardless of which model is used. These results could be mainly ascribed to a certain system
303   deviation between the comparison data of ECMWF and the GNSS tomographic data. Besides, due to less
304   voxels with GNSS rays penetration in the lower layers, the observations are too insufficient to get good
305   accuracy. Figure 2 also shows that the water vapor content in the bottom region is so abundant and
306   changeable that tomography results from models could not reflect it accurately. These above reasons lead
307   to large bias and RMSE values in the bottom tropospheric area.

308   **Table 2.** Statistics of two models' tomography accuracy with respect to ECMWF data in the spatial distribution scenario
309   for the experimental period (Unit: g/m^3).

Layer	bias		RMSE		RMSE Improvement Percentage
	Traditional model	Improved model	Traditional model	Improved model	
1	-7.81	-7.65	8.17	8.00	2.06%
2	-3.52	-3.42	3.95	3.83	3.14%
3	-0.90	-0.80	1.66	1.60	4.05%
4	0.72	0.61	1.39	1.36	2.00%
5	1.62	1.58	1.87	1.83	2.28%
6	1.95	1.77	2.10	2.09	0.39%
7	1.98	1.90	2.25	2.20	2.07%
8	1.76	1.68	2.15	2.10	2.32%
9	1.62	1.60	2.06	2.04	1.10%
10	1.34	1.11	1.85	1.47	20.68%
11	1.04	0.87	1.60	1.25	21.75%
12	0.74	0.61	1.26	0.96	23.67%
13	0.44	0.38	0.71	0.58	18.36%
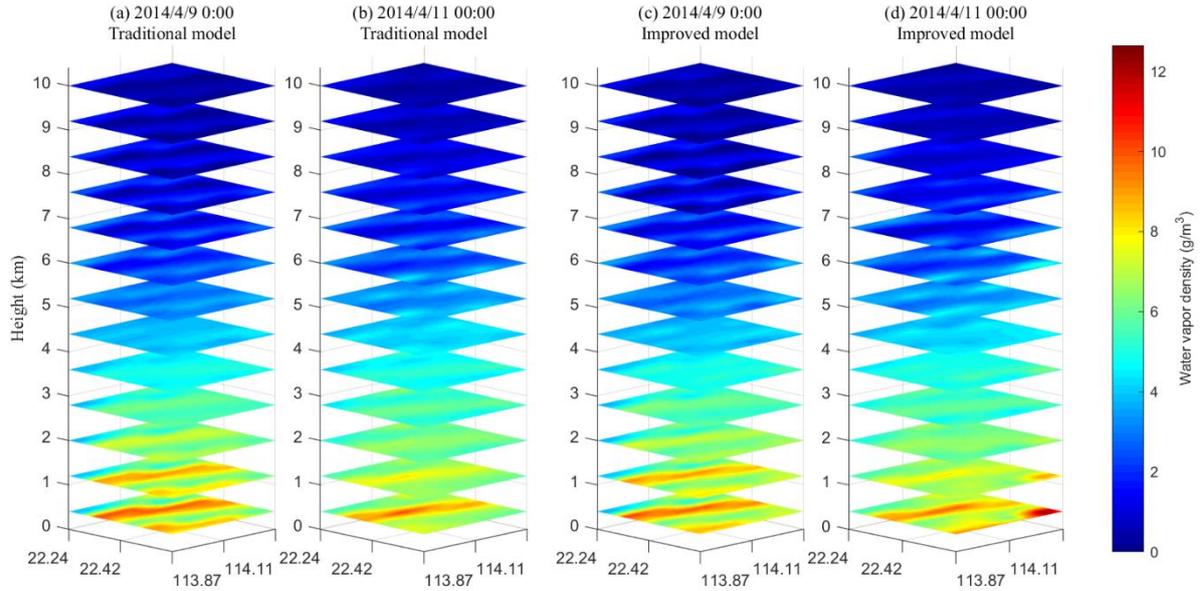
310 **Figure 2.** The layered maps of the water vapor density from **(a) (b)** the traditional model and **(c) (d)** the improved

311 model at specific epochs, **(a) (c)** 0:00 UTC 9 April 2014 and **(b) (d)** 0:00 UTC 11 April 2014.

312 *4.2. The accuracy information of the everyday distribution scenario*

313   To prove whether the accuracy of the improved model is better than that of the traditional model on

314 the everyday time scale, the RMSE improvement percentage is obtained from all ECMWF comparative

315 points (a total of 12) at two epochs each day, using both the layered optimal polynomial functions and the

316 traditional method. Figure 3 shows that the percentage of RMSE improvement per day is mostly positive,

317 and the percentage of April 11th can even approach 12%, indicating that the improvement seems to be

318 appreciable. This improvement shows that the accuracy of the improved model is mostly superior to that of

319 the traditional model in everyday distribution; however, on April 7, April 9 and April 15, the RMSE

320 improvement percentage is negative. This might be due to the heavy showers bringing rapid water vapor

321 changes from April 7 to April 8 and on April 14, which is difficult to fit the polynomial function well with

322 the unstable water vapor. However, since negative percentages do not exceed -1%, the accuracy of the

323 improved model could be considered basically equivalent to that of the traditional model for these four

324 days.
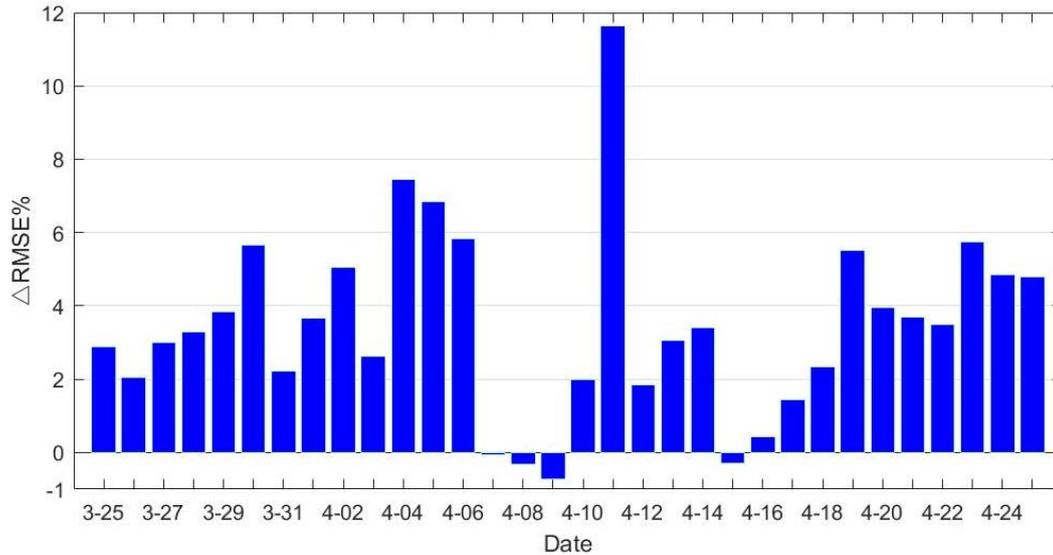
325

326 **Figure 3.** Everyday distribution statistics of daily RMSE improvement percentage between 25 March and 25 April,

327 2014.

328   In addition, the overall RMSE and bias of the residuals are obtained from the ECMWF comparative

329 points (a total of 12) in two epochs under the entire everyday distribution scenario. The statistical results

330 are shown in Table 3 below.

331 **Table 3.** Statistics of two models' tomography accuracy with respect to ECMWF data in the everyday distribution

332 scenario for the experimental period (Unit: g/m^3).

Statistics type	Traditional model	Improved model	RMSE improvement percentage
RMSE	2.97	2.87	3.44%
bias	0.07	0.02	

333   Table 3 shows that the RMSE obtained by the improved model is smaller by 3.44% compared to that

334 of the traditional one. The bias of the improved model more closes to zero, indicating that the improved

335 model has better stability and less systematic deviation from the comparative data. The better accuracy

336 shows the superiority of the improved model.

337 *4.3. The accuracy information of rainy and non-rainy scenarios*

338   To further analyze the reliability of the improved model compared with the traditional model in

339 different weather conditions, according to the distribution of rainy days in Table 1, all the rainy days data

340 and non-rainy days data are used separately for tomography to obtain the RMSE and bias of the residuals

341 under corresponding weather conditions. The number of matching points is still 12 (see Fig. 1). The overall

342 statistical results are shown in Table 4.

343 **Table 4.** Statistics of two models' tomography accuracy with respect to ECMWF data in the rainy scenario and the non-

344 rainy scenario for the experimental period (Unit: g/m^3).

(a) The overall rainy scenario statistics			
Statistics type	Traditional model	Improved model	RMSE improvement percentage
RMSE	3.05	2.94	3.68%
bias	0.05	-0.01	
(b) The overall non-rainy scenario statistics			
Statistics type	Traditional model	Improved model	RMSE improvement percentage
RMSE	2.89	2.80	3.21%
bias	0.10	0.04	

345   Table 4 (a) shows that the RMSE and bias of the residuals calculated by the improved model are better

346 than those of the traditional model using rainy days' data. The RMSE of the improved model is 3.68%

347 better than that of the traditional model, indicating the accuracy of the new model is superior. The improved

348 model bias closes more to zero than that of the traditional one, which means the improved model has an

349 increase in stability and a reduction in the system error. Using non-rainy days' data, the RMSE and bias of

350 the residuals calculated by the improved model are also better than those of the traditional model (see Table

351 4 (b)). The RMSE improvement percentage is 3.21%, also indicating the improved model has enhanced

352 accuracy. Besides, the improved model bias is more close to zero, making the system error weakened. Table

353 4 also shows that the RMSE improvement percentage of the rainy-day is better than that of the non-rainy

354 days. This finding shows that the improved model is more suitable for obtaining the tomographic results

355 when heavy water vapor changes occur.

356 *4.4. The accuracy information of voxels with and without GNSS rays penetrating scenarios*

357   In the traditional pixel-based water vapor tomography model, the water vapor density in the voxels

358 without GNSS rays passing through depends on the accuracy of the water vapor density in the adjacent

359 voxels with GNSS rays penetration. However, the improved model uses the layered optimal polynomial

360 functions for overall fitting to obtain the water vapor density in voxels without penetrating GNSS rays. To

361 determine if the layered optimal polynomial function of the improved model contributes better to the

362 accuracy of the water vapor density, the scenarios of voxels with and without GNSS rays penetration as

363 described in section 3.2 were designed. After obtaining the RMSE and bias of the residuals using the

364 improved and traditional tomography models separately under designed scenarios, the overall accuracy

365 information of voxels with and without GNSS rays penetrating shows in Table 5.

366 **Table 5.** Statistics of two models' tomography accuracy with respect to ECMWF data in the voxels with and without

367 penetrating GNSS rays for the experimental period (Unit: g/m^3).

(a) The overall scenario statistics of voxels without rays penetrating			
Statistics type	Traditional model	Improved model	RMSE Improvement Percentage
RMSE	3.40	3.20	5.88%
Bias	1.59	1.51	
(b) The overall scenario statistics of voxels with rays penetrating			
Statistics type	Traditional model	Improved model	RMSE Improvement Percentage
RMSE	3.27	3.24	1.00%
bias	1.70	1.65	

368   Table 5 (a) shows that the RMSE and bias of the residuals calculated by the improved model are better

369 than those of the traditional model in the scenario of voxels without GNSS rays penetrating. Moreover the

370 RMSE of improved tomography model is 5.88% better than that of the traditional model, and the bias

371 decreased from 1.59 to 1.51 g/m^3. To a certain extent, results show that the improved model is more

372 advantageous for obtaining the water vapor density from the voxels without GNSS rays penetrating, which

373 is consistent with the initial hypothesis: the traditional model uses empirical constraint equations in section

374 2.1.2, Eq. (7), which is unable to well represent the actual distribution of the water vapor density from

375 voxels without GNSS rays penetrating. However, the improved model uses the relatively accurate water

376 vapor density from voxels with GNSS rays penetrating as the observation values to further fit the water

377 vapor density in voxels without GNSS rays penetrating. Therefore, the improved model can better reflect

378 the actual layered situation of continuous water vapor changes, and the accuracy is naturally better. What's

379 more, in the scenario of voxels with GNSS rays penetrating, the RMSE and bias obtained by the improved

380 model are also superior to those of the traditional models, see Table 5 (b). The RMSE calculated by the

381 improved model is 1% higher than that of the traditional model, and the bias reduced from 1.7 to 1.65 g/m^3,

382 which could prove the reliability of the improved model.

383   In order to double-check if the improved model in the scenario of voxels without GNSS rays

384 penetration shows a better result in the vertical water vapor distribution, the water vapor density profiles

385 for different altitudes at specific times are given in Fig. 4. Two times (0:00 UTC 11 April 2014 and 12:00

386 UTC 11 April 2014) are chosen for they correspond to the maximum percentage of RMSE improvement

387 during the experiment period of 32 days. Figure 4 shows that in the scenario of voxels without GNSS rays

388 penetration, the water vapor profile of the improved model better matches that of ECMWF data than the

389 traditional model, especially in the bottom layers, which again implies that the water vapor density derived

390 from the improved model is superior to that of the traditional one in the scenario of voxels without GNSS

391 rays penetrating.
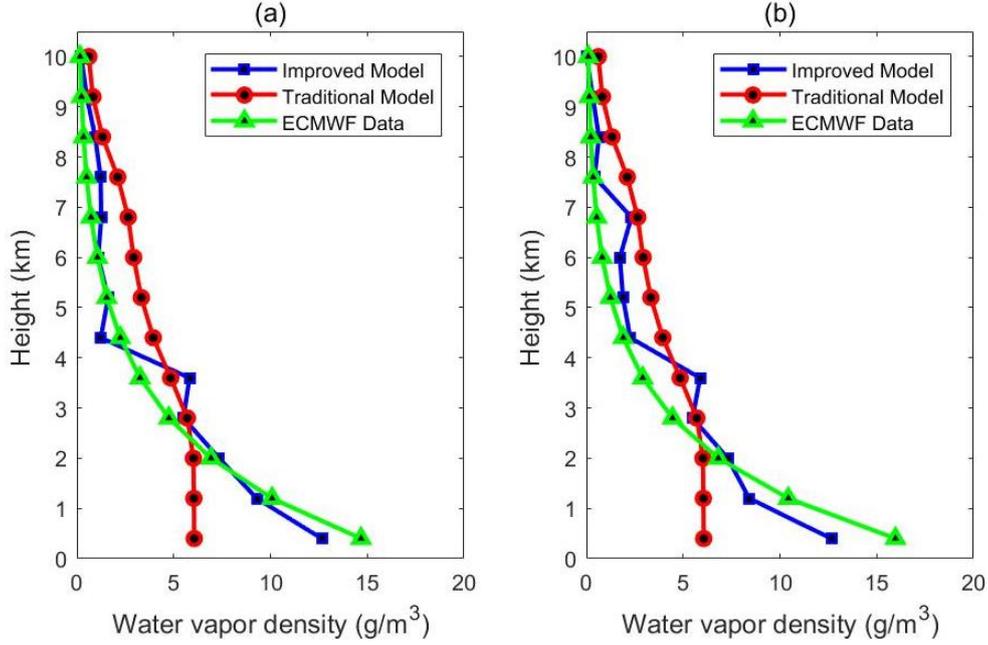
392 **Figure 4.** Water vapor profiles derived from ECMWF and two models in the scenario of voxels without penetrating
393 GNSS rays, **(a)** and **(b)** are periods of 0:00 UTC 11 April 2014 and 12:00 UTC 11 April 2014, respectively.

394   Furthermore, to compare directly the vertical accuracy of the water vapor density derived from
395 different altitudes in the scenario of voxels without penetrating GNSS rays, the tomographic results (25
396 March 2014 to 25 April 2014) from two different tomography models are analyzed. Figure 5 shows the
397 percentage of RMSE improvement and the relative error of the water vapor density changing with altitudes.
398 The percentage of RMSE improvement in Fig. 5 is defined as the same as Eq. (16), and the relative error is
399 defined by using the Eq. (17).

400
$$RE = \frac{\rho - \rho_{ECMWF}}{\rho_{ECMWF}} \qquad (17)$$

401   where RE is the relative error, ρ represents the water vapor density derived from the traditional or

402 improved tomography model, and ρ_{ECMWF} is the water vapor density derived from ECMWF grid data.

403   It can be observed in Fig. 5 that in the scenario of voxels without GNSS rays penetration the percentage
404 of RMSE improvement is positive in lower layers while negative in some middle and upper layers, which
405 could prove that the improved model enhances the accuracy of tomography results in most layers when
406 there are seldom voxels with GNSS rays penetrating especially in the bottom layers. Due to the lack of
407 GNSS observation data, the bottom accuracy of tomographic results is generally low. In addition, Figure 5
408 shows in the scenario of voxels without GNSS rays penetration, the relative error begins to decrease with
409 the altitude and then increases above 3 km. When the altitude is higher, the relative error becomes larger
410 because of the small water vapor values in the upper layers, a very tiny difference could cause a large
411 relative error between the models and the ECMWF data.
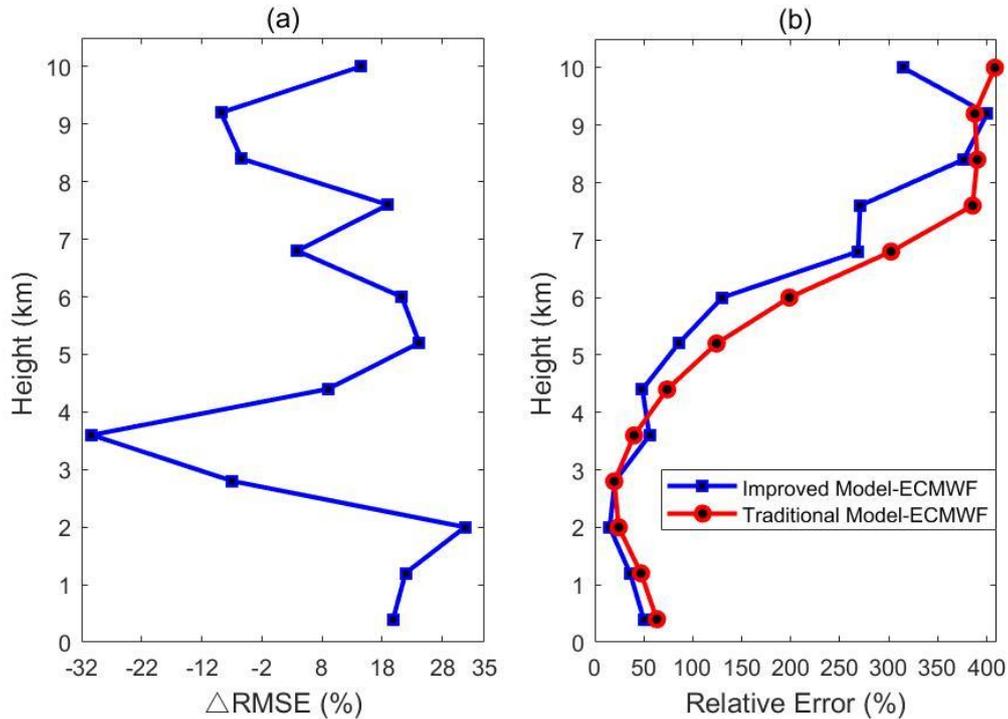
Figure 5. In the scenario of voxels without GNSS rays penetration **(a)** the percentage of RMSE improvement and **(b)** the relative error change with height (the blue curve and red curve are derived from the differences between the profiles of the improved model, the traditional model and ECMWF grid data, separately for 64 epochs from 25 March 2014 to 25 April 2014).

5. Water vapor comparison with radiosonde data

As radiosonde data can provide fairly accurate vertical profiles of tropospheric water vapor (Niell et al., 2001), in this paper, the water vapor profiles derived from radiosonde data, as a reference, are used to validate the tomographic results from two models for showing if the improved model would be more efficient than the traditional one. In Hong Kong, there is one radiosonde station located at King's Park (shown in Fig. 1) where radiosonde balloons are launched twice daily at 0:00 and 12:00 UTC, respectively. Water vapor profiles derived from the improved model and the traditional model for the location of the radiosonde station are compared with that derived from radiosonde data at 00:00 and 12:00 UTC daily for the experimental period of 32 days. The overall statistical results are shown in Table 6. The RMSE and the bias of the improved model are 1.03 and -0.06 g/m^3, respectively, and the values of the traditional model are 0.82 and -0.17 g/m^3, respectively, which indicates that the RMSE of the improved model is not as good as the traditional model while the bias of the improved model is a little better than that of the traditional one. The reason for poor accuracy of the improved model could be due to systematic differences between the training source ECMWF data and the radiosonde data. Besides, shown in Fig.1, the location of the radiosonde station is close to one GNSS station (HKSC), leading to the voxels for the location of the radiosonde station having GNSS rays penetration. Since the improved model has advantages of obtaining water vapor density just from voxels without GNSS rays penetration, this situation cannot show the superiority of the improved model.

434 **Table 6.** Statistics of two models' tomography accuracy with respect to radiosonde data for the experimental period
435 (Unit: g/m³).

Statistics type	Traditional model	Improved model
RMSE	0.82	1.03
bias	-0.17	-0.06

436   In addition, water vapor profiles obtained by two models and radiosonde data are compared for the
437 specific two epochs at 0:00 UTC 25 March 2014 and 0:00 UTC 7 April 2014, shown in Fig. 6. Those two
438 times are selected because they correspond to the non-rainy day and heavy rainfall day, which could be
439 more comprehensive and representative for the comparison results of water vapor profiles. It can be seen
440 from Fig.6 that two models in the non-rainy day match the radiosonde data a little better than that in the
441 rainy day. The traditional model shows better comparison results in upper layers than that of the improved
442 model while the two models have almost the same comparison results in the middle and lower layers. The
443 reason for poor performance in the lower layers might due to abundant water vapor in the bottom
444 troposphere as well as the division of the vertical resolution. Compared to the radiosonde data, with almost
445 the same accuracy and profile matching results as the traditional model, the improved model still has the
446 advantage of the convenient and efficient expression.
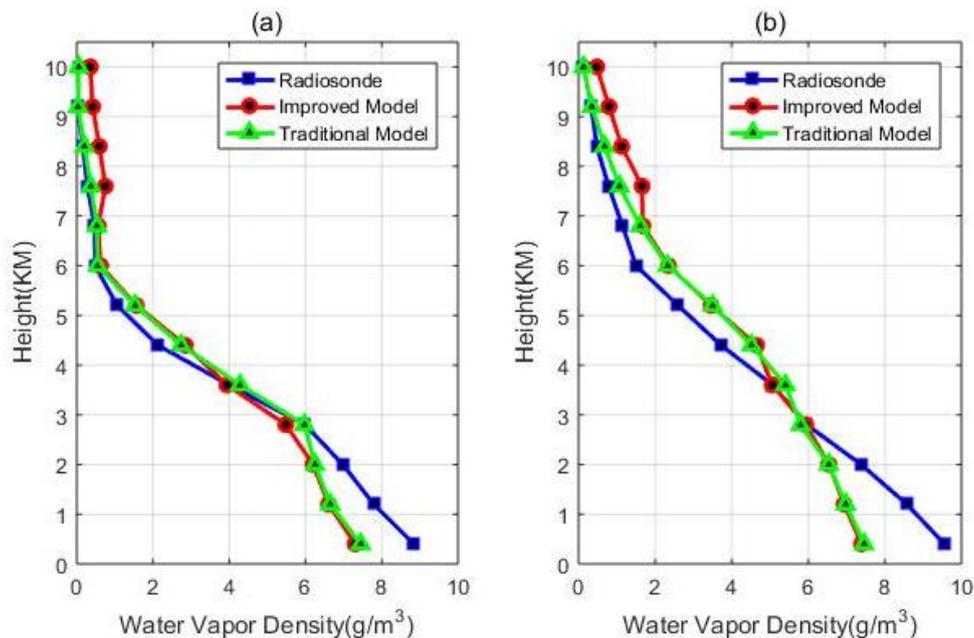
447

448 **Figure 6.** Water vapor profile comparison derived from different tomographic methods and radiosonde, **(a)** a non-rainy
449 day at 0:00 UTC 25 March 2014, **(b)** a rainy day at 0:00 UTC 7 April 2014.

450 **6. SWV comparison**

451   In order to further verify the reliability of the improved model, five days are randomly selected from
452 different weather conditions to make assessments on the reconstructed SWVs of two models (see Table 7).
453 The comparison between measured SWVs and the ones derived from tomography results of two models is
454 performed and the average RMSE and bias are shown in Table 8. The RMSE and bias of SWVs obtained
455 from tomography results of two models are almost the same under different weather conditions, which
456 indicates the reconstructed SWVs of the improved model has the similar accuracy with that of the traditional
457 one. Since the improved model has the advantage in expressing the water vapor distribution more

458 expediently, the similar accuracy of two models in SWVs comparison shows the reliability and superiority

459 of the improved model.

460 **Table 7.** Statistics of two models' accuracy of SWVs for different weather conditions for 5 days (Unit: mm).

Data	3.30		4.2		4.9		4.13		4.25	
Condition	Thunderstorms turn to heavy rain		Showers, reports of hail in some areas		Non rainy		Sunny		Cloudy turns to the rain	
Model	Traditional	Improved	Traditional	Improved	Traditional	Improved	Traditional	Improved	Traditional	Improved
RMS	10.14	10.28	15.03	15.48	2.47	2.56	8.22	8.55	12.21	12.84
Bias	-2.67	-3.03	-1.94	-2.08	0.14	-0.06	-1.51	-1.54	-3.40	-3.89

461 **Table 8.** Statistics of two models' average accuracy of SWVs for the experimental period (Unit: mm).

Statistics type	Traditional model	Improved model
RMSE	9.63	10.06
bias	-1.89	-2.15

462 **7. Conclusion**

463 In this paper, an improved pixel-based water vapor tomography model has been proposed, which is

464 much more concise and convenient in expression than the traditional one. Only using the layered optimal

465 polynomial coefficients, the three-dimensional water vapor distribution in the tomography region could be

466 described. By using the SatRef GNSS network observation data in Hong Kong between 25 March and 25

467 April, 2014, the RMSE and bias have been assessed in 6 scenarios. The scenarios include the spatial

468 distribution scenario and the everyday distribution scenario, the rainy scenario and the non-rainy scenario,

469 and the voxels with and without GNSS rays penetrating scenarios. The results demonstrate that in either

470 case, the RMSE and bias of the improved model are better than that of the traditional model. Among these

471 scenarios, when there are voxels without GNSS rays penetrating, the RMSE improvement percentage can

472 be significantly increased up to 5.88%, which shows that the improved model is more advantageous for

473 obtaining the water vapor density from voxels without GNSS rays penetration. Using radiosonde data for

474 evaluation, it is proved that with the almost similar accuracy the improved model is more efficient in

475 expression than the traditional one. However, some shortcomings still remain in the improved model. For

476 example, more or less the water vapor accuracy of the improved model is still affected by the traditional

477 model, and the layered optimal polynomial functions are limited by the size of the tomographic area and

478 the situation of dividing voxels. In the future, the function-based water vapor tomography model, which is

479 free from the above limitations, should be studied. It is expected that the function-based water vapor

480 tomography model will be more conveniently used when the expression parameters of the function part

481 could be obtained directly from SWVs.

482 **Acknowledgments:** The authors would like to thank ECMWF for providing access to the layered meteorological data.
483 The Lands Department of HKSAR is also acknowledge for providing GPS data from the Hong Kong Satellite
484 Positioning Reference Station Network (SatRef) and corresponding meteorological data.

485 **Conflicts of Interest:** The authors declare that they have no conflict of interest.

486 **References**

487 Aghajany, S. H. and Amerian, Y.: Three dimensional ray tracing technique for tropospheric water vapor

488 tomography using GPS measurements, J. Atmos. Sol.-Terr. Phys., 164:81-88, 2017.

489 Alber, C., Ware, R., Rocken, C., and Braun, J. J.: Obtaining single path phase delays from GPS double

490   differences, Geophys. Res. Lett., 27, 2661–2664, 2000.

491   Baltink, H. K., Marel, H. V. D., and Der Hoeven, A. V.: Integrated atmospheric water vapor estimates from

492   a regional GPS network, J. Geophys Res-Atmos., 107, ACL 3-1–ACL 3-8, 2002.

493   Bender, M., Stosius, R., Zus, F., Dick, G., Wickert, J., and Raabe, A.: GNSS water vapour tomography –

494   Expected improvements by combining GPS, GLONASS and Galileo observations, Adv. Space Res., 47,

495   886-897, 2011.

496   Bevis, M., Businger, S., Chiswell, S. R., Herring, T. A., Anthes, R. A., Rocken, C., and Ware, R.: GPS

497   meteorology: mapping zenith wet delays onto precipitable water, J. Appl. Meteorol., 33, 379-386, 1994.

498   Bi, Y., Mao, J., and Li, C.: Preliminary results of 4-D water vapour tomography in the troposphere using

499   GPS, Adv. Atmos. Sci., 23, 551–560, 2006.

500   Bock, O., Keil, C., Richard, E., Flamant, C., and Bouin, M.: Validation of precipitable water from ECMWF

501   model analyses with GPS and radiosonde data during the MAP SOP, Q. J. Roy. Meteorol. Soc., 131, 3013-

502   3036, 2005.

503   Braun, J. J., Rocken, C., Meertens, C., and Ware, R.: Development of a Water Vapor Tomography System

504   Using Low Cost L1 GPS Receivers, in: Ninth ARM Science Team Meeting Proceedings, San Antonio,

505   Texas, 22-26 March 1999, 1-6, 1999.

506   Braun, J. J., Rocken, C., and Liljegren, J. C.: Comparisons of line-of-sight water vapor observations using

507   the global positioning system and a pointing microwave radiometer, J. Atmos. Ocean. Tech., 20, 606-612,

508   2003.

509   Braun, J. J.: Remote sensing of atmospheric water vapor with the global positioning system, Ph.D. thesis,

510   University of Colorado, 2004.

511   Cao, Y.: GPS Tomographying Three-Dimensional Atmospheric Water Vapor and Its Meteorological

512   Applications, Ph.D. Thesis, The Chinese Academy of Sciences, Beijing, China, 2012.

513   Chen B. and Liu Z.: Voxel-optimized regional water vapor tomography and comparison with radiosonde

514   and numerical weather model, J. Geodesy, 88, 691-703, 2014.

515   Ding, N., Zhang, S. B., Wu, S.Q., Wang, X. M., and Zhang, K. F.: Adaptive node parameterization for

516   dynamic determination of boundaries and nodes of GNSS tomographic models, J. Geophys. Res-Atmos.,

517   123, 1990-2003, 2018.

518   Dong Z. and Jin S.: 3-D Water Vapor Tomography in Wuhan from GPS, BDS and GLONASS Observations,

519   Remote Sens., 10(1):62, 2018.

520   Emardson, T. R., Elgered, G., and Johansson, J. M.: Three months of continuous monitoring of atmospheric

521   water vapor with a network of Global Positioning System receivers, J. Geophys. Res., 103, 1807-1820,

522   1998.

523   Flores, A., Ruffini, G., and Rius, A.: 4D tropospheric tomography using GPS slant wet delays, Ann.

524   Geophys. Ger., 18, 223-234, 2000.

525   Guo, J., Yang, F., Shi, J., and Xu, C.: An Optimal Weighting Method of Global Positioning System (GPS)

526   Troposphere Tomography, IEEE J-STARS., 9(12), 5880-5887, 2016.

527   Herring, T. A., King, R. W., and McClusky, S. C.: Documentation of the GAMIT GPS Analysis Software

528   release 10.4. Department of Earth and Planetary Sciences, Massachusetts Institute of Technology,

529   Cambridge, Massachusetts, 2010.

530   Hirahara K.: Local GPS tropospheric tomography, Earth Planets Space, 52, 935-939, 2000.

531   Liu, Y., Chen, Y., and Liu, J.: Determination of weighed mean tropospheric temperature using ground

532   meteorological measurements, Geospatial Inf. Sci., 4, 14-18, 2001.

533 Macdonald, A. E., Xie, Y., and Ware, R. H.: Diagnosis of Three-Dimensional Water Vapor Using a GPS
534 Network, Mon. Weather Rev., 130, 386-397, 2002.

535 Marel, H. V. D.: Virtual GPS reference stations in the Netherlands, in: Proceedings of ION GPS-98,
536 Nashville, TN, 15-18 September, pp. 49-58, 1998.

537 Niell, A. E., Coster, A. J., Solheim, F. S., Mendes, V. B., Toor, P. C., Langley, R. B., and Upham, C. A.:
538 Comparison of measurements of atmospheric wet delay by radiosonde, water vapour radiometer, GPS, and
539 VLBI, J. Atmos. Ocean. Tech., 18, 830–850, 2001.

540 Nilsson, T. and Gradinarsky, L.: Water vapor tomography using GPS phase observations: simulation results,
541 IEEE T. Geosci. Remote, 44, 2927-2941, 2006.

542 Perler, D., Geiger, A., Hurter, F.: 4D GPS water vapor tomography: new parameterized approaches, J.
543 Geodesy, 85, 539-550, 2011.

544 Rocken, C., Van Hove, T., and Ware, R.: Near real‐time GPS sensing of atmospheric water vapor, Geophys.
545 Res. Lett., 24, 3221-3224, 1997.

546 Rohm, W. and Bosy, J.: Local tomography troposphere model over mountains area, Atmos. Res., 93, 777-
547 783, 2009.

548 Rohm, W., Zhang, K., and Bosy, J.: Limited constraint, robust Kalman filtering for GNSS troposphere
549 tomography, Atmos. Meas. Tech., 6, 1475-1486, 2014.

550 Saastamoinen, J.: Atmospheric Correction for the Troposphere and Stratosphere in Radio Ranging Satellites,
551 The use of Artificial Satellites for Geodesy, 15, 247-251, 1972.

552 Seko, H., Shimada, S., Nakamura, H., and Kato, T.: Three-dimensional distribution of water vapor
553 estimated from tropospheric delay of GPS data in a mesoscale precipitation system of the Baiu front, Earth
554 Planets Space, 52, 927-933, 2000.

555 Troller, M., Burki, B., Cocard, M., Geiger, A., and Kahle, H. G.: 3-D refractivity field from GPS double
556 difference tomography, Geophys. Res. Lett., 29, 2-1–2-4, 2002.

557 Vollach, U., Buecherl, A., Landau, H., Pagels, C., Wagner, B.: Multi-Base RTK Positioning Using Virtual
558 Reference Stations, in: Proceedings of ION GPS-2000, Salt Lake City, 19-22 September 2000, 123-131,
559 2000.

560 Weckwerth, T. M., Parsons, D. B., Koch, S. E., Moore, J. A., Lemone, M. A., Demoz, B., Flamant, C.,
561 Geerts, B., Wang, J., and Feltz, W. F.: An overview of the international H2O project (IHOP_2002) and some
562 preliminary highlights, B. Am. Meteorol Soc., 85, 253-277, 2004.

563 Yao, Y. B., Zhao, Q. Z., and Zhang, B.: A method to improve the utilization of GNSS observation for water
564 vapor tomography, Ann. Geophys., 34, 143-152, https://doi.org/10.5194/angeo-34-143-2016, 2016.

565 Yao, Y., Chen, P., Zhang, S., and Chen, J.: A new ionospheric tomography model combining pixel-based
566 and function-based models, Adv. Space Res., 52, 614-621, 2013.

567 Zhang B., Fan Q.*, Yao Y., Xu C. and Li X,: An Improved Tomography Approach Based on Adaptive
568 Smoothing and Ground Meteorological Observations, Remote Sens., 9,886, 2017, DOI:10.3390/rs9090886

569 Zhao, Q. and Yao, Y.: An improved troposphere tomographic approach considering the signals coming from
570 the side face of the tomographic area, Ann. Geophys., 35, 87-95, https://doi.org/10.5194/angeo-35-87-2017,
571 2017.

572 Zhao, Q., Yao, Y., Yao, W., and Xia, P.: An optimal tropospheric tomography approach with the support of
573 an auxiliary area, Ann. Geophys., 36, 1037-1046, https://doi.org/10.5194/angeo-36-1037-2018, 2018.